Influence of microwave-assisted hydrothermal treatment time on the crystallinity, morphology and optical properties of ZnWO₄ nanoparticles: Photocatalytic activity

N.F. Andrade Neto[a,*], T.B.O. Nunes[a], M. Li[c], E. Longo[b], M.R.D. Bomio[a], F.V. Motta[a]

[a] LSQM, Laboratory of Chemical Synthesis of Materials, Department of Materials Engineering, Federal University of Rio Grande do Norte, UFRN, P.O. Box 1524, Natal, RN, Brazil
[b] CDMF-UFSCar, Universidade Federal de São Carlos, P.O. Box 676, São Carlos, SP, 13565-905, Brazil
[c] IFSC, USP, Av. Trabalhador São Carlense, 400, CEP, 13566-590, São Carlos, SP, Brazil

ABSTRACT

In this work, zinc tungstate (ZnWO₄) nanoparticles were obtained by microwave-assisted hydrothermal method at 140 °C and 2 atm. The hydrothermal treatment time was varied at 0, 5, 10, 30, 60 and 120 min. The nanoparticles were characterized by X-ray diffraction (XRD), Fourier transform infrared spectroscopy (FTIR), scanning electron microscopy (SEM), transmission electron microscope (TEM), high-resolution transmission electron microscope (HRTEM), X-ray fluorescence (FRX), nitrogen adsorption by Brunauer-Emmett-Teller method (BET), UV–Visible spectroscopy (UV–Vis) and Photoluminescence (PL) properties. The adsorptive and photocatalytic properties were estimated against methylene blue (MB - cationic) and methyl orange (MO - anionic) dyes. The diffractograms show that the larger hydrothermal treatment time, anhigher the powders crystallinity. The BET and SEM analysis indicate that the increase in hydrothermal time does not interfere significantly in nanoparticles size but reduces their porosity. The change in the surface area is consistent with the adsorption tests, where the increase of the hydrothermal treatment time reduces the adsorption against the MB and MO dyes. However, increasing the hydrothermal treatment time provides an increase in photocatalytic activity.

1. Introduction

Metallic tungstates have been gaining increasing attention due to wolframite structures, which are characterized by good optical properties and high chemical and thermal stability due to their intrinsic structural defects caused by your electronic configuration ($d^{10}s^2d^0$) [1,2]. These characteristics make these materials widely reported in the literature for various applications, such as optical fibers, diodes, sensors and photocatalysis [3–6]. Due to the absence of symmetry, tungstates with monoclinic structures are more suitable for photocatalytic applications, being easier to insert defects [7]. Among these, the zinc tungstate (ZnWO₄) stands out because it has ZnO₆ and WO₆ octahedra connected by shared oxygen atoms [8].

ZnWO₄ can be obtained by different methods, such as sol-gel, spray-pyrolysis, sonochemical, hydrothermal, among others [6,9–13]. The microwave-assisted hydrothermal treatment stands out due to provide homogeneous temperature throughout the solution, generating a fast crystallization rate and requiring low times to obtain the crystalline structure [14,15]. He et al. [16] performed conventional hydrothermal synthesis for 24 h under 180 °C and only obtained the crystalline phase of ZnWO₄ after subsequent calcination at 600 °C for 2 h. Siriwong et al. [6] showed the influence of pH on the amount of ZnWO₄ and ZnO phases by the hydrothermal method for 24 h under 200 °C. Qureshi et al. [17] obtained ZnWO4 decorated graphene oxide by the hydrothermal method under 180 °C for 6 h, followed by calcination at 180 °C for 4 h. Recently, Carvalho et al. [18] reported the ZnO:ZnWO₄ heterostructure obtained by hydrothermal method at 200 °C for 12 h with rod morphology and high photocatalytic properties. Thus, ZnWO₄ obtained by the hydrothermal method is widely reported in the literature, but at long times and requiring further heat treatment. In addition, these methodologies produce ZnWO₄ with low photocatalytic activity, where its use requires some improvement, such as doping or impregnation [19–21].

Among the problems encountered in the ZnWO4 structures, there is low absorption at wavelengths near the visible region, absorbing practically radiations in the UV–Vis region [22]. In addition, due to

---

their electronic configuration, they have a high electron/hole (e^-/h^+) pairs recombination rate [23]. Thus, in this work, we sought to study the $ZnWO_4$ nanoparticles obtainment in short hydrothermal treatment times and without the need for further thermal treatments. For this, the temperature (140 °C) and pressure (2 atm) were fixed and the permanence time in microwave-assisted hydrothermal treatment was varied between 5 and 120 min, aiming to analyze the effect of the treatment time on the crystalline, morphological, adsorptive and photocatalytic properties.

2. Materials and methods

2.1. Synthesis

$Zn(NO_3)_2 \cdot 6H_2O$ (Sigma-Aldrich, 98%), $Na_2WO_4 \cdot 2H_2O$ (Synth, 99.5%), PVP (polyvinylpyrrolidone, Vetec) and deionized water were used as precursor materials. For this, 1 mM of $Zn(NO_3)_2 \cdot 6H_2O$ and 5 mM of PVP were dissolved in 40 mL of deionized water and kept under stirring, forming solution 1. Solution 2 was formed by 1 mM $Na_2WO_4 \cdot 2H_2O$, 5 mM PVP and 40 mL deionized water, also maintained under stirring. After complete solubilization, solution 1 was poured into solution 2, with the precipitation of a white solid, which was washed with deionized water and dried in an oven (100 °C) for 24 h, being referred to as ZW0.

This experimental procedure was repeated and the precipitate was transferred to a Teflon reactor inside the autoclave under temperature of 140 °C and pressure of 2 atm, where it was treated in microwave-assisted hydrothermal bath (2.45 GHz and a maximum power of 800 W) at times of 5, 10, 30, 60 and 120 min, forming samples AW5, AW10, AW30, AW60 and AW120, respectively. After the hydrothermal treatment, the precipitate was washed with deionized water and dried at 100 °C for 24 h.

2.2. Characterization

The crystalline structure of the powders was characterized by X-ray diffraction using CuKα radiation (1.5418 Å) using the Shimadzu diffractometer (XRD-6000) operating in Rietveld routine mode with step of 0.02° and 1°/min speed. The chemical composition was determined by X-ray fluorescence (XRF) using the Shimadzu EDX-720 spectrometer. The morphology of the powders was studied by field emission scanning electron microscopy (SEM) under Supra 35 zeiss microscope. The nanoparticles mean diameter was estimated using the ImageJ software [24] using SEM images with different magnifications. Transmission electron microscopy (TEM) and high-resolution transmission electron microscopy (HRTEM) were performed in FEI TECNAI G2 F20 microscope operating at 200 kV. The surface area was estimated by the Brunauer-Emmett-Teller method (BET) by adsorption of N_2 in the Bel Japan, INC equipment. Fourier transform infrared spectroscopy was performed on the IRTracer-100 (Shimadzu) equipment between 400 and 4000 cm^{-1} operating in transmittance mode. Spectroscopy in the visible ultraviolet region (UV–Vis) was used in the diffuse reflectance mode. The Kubelka-Munk function [25] was used to convert the data to absorbance and the Wood and Tauc equation [26] was applied for gap band estimation (Egap). The photoluminescence (PL) measurements were obtained using a 325 nm laser at room temperature in a Mosospec 27 monochromator (Thermal Jarrel Ash, USA) coupled to an argon laser photomultiplier (Coherent innova 90 K, USA).

2.3. Photocatalytic activity

The photocatalytic activity was estimated against methylene blue (MB) and methyl orange (MO) dyes, both at pH 5. 0.05 g of the material was placed in contact with 50 mL of the aqueous solution of MB (cationic, 10^{-5} mol L^{-1} concentration) and kept under stirring for 20 min to eliminate the adsorbent effects. After that time, six UVC lamps (TUV
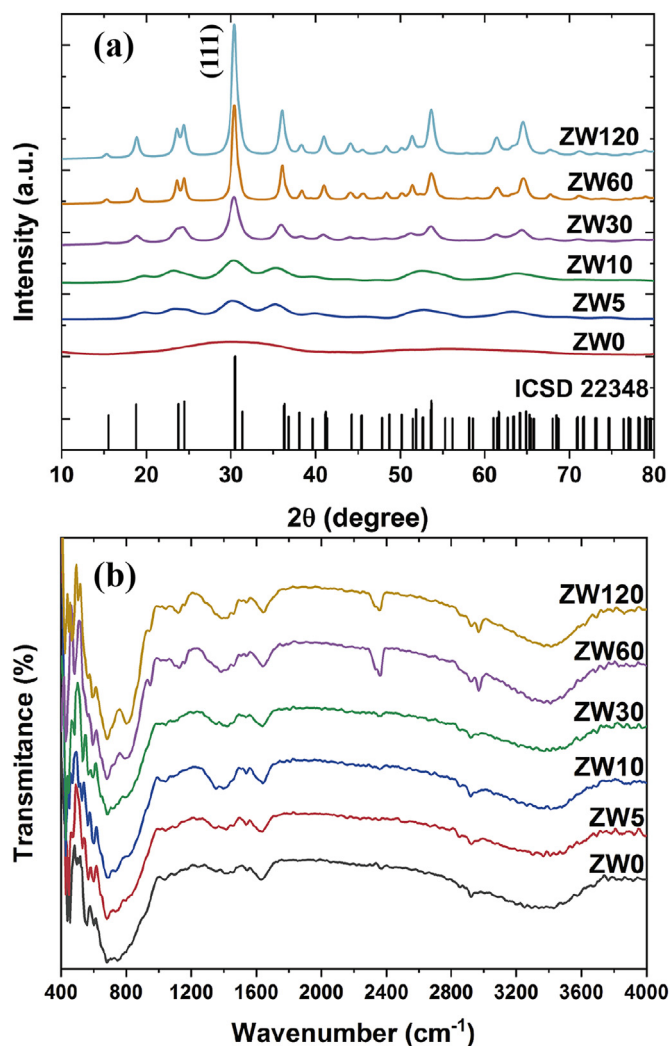

Fig. 1. (a) Diffractograms and (b) FTIR spectra for $ZnWO_4$ samples.

Philips, 15 W) illuminated the solutions for 120 min. Similar procedure was performed for MO dye (anionic, 10^{-5} mol L^{-1} concentration). The photocatalytic activity was then determined by the variation of the dyes absorption bands in Shimadzu UV-2600 spectrophotometer.

The mechanism acting on the photocatalytic process was determined by the use of charge, electron (e^-) and hole (h^+), and hydroxyl radical (·OH) sequestrants. For this, isopropyl alcohol (1 mL alcohol/100 mL dye), EDTA (7.2 mg EDTA/100 mL dye) and $AgNO_3$ (8.5 mg $AgNO_3$/100 mL dye) were used to suppress the action of hydroxyl radicals (·OH), positive charges (h^+) and negative charges (e^-), respectively.

The reuse tests were performed against MB dye with three consecutively cycles, without any treatment. For this, the powders were separated by centrifugation after analysis and dried in atmosphere air. After dried, the powders were weighed and the relationship between catalytic/dye (1 mg/1 mL) was maintained.

3. Results and discussion

Fig. 1 shows the X-ray diffractograms of the $ZnWO_4$ powders obtained at different times of microwave-assisted hydrothermal treatment. For ZW0 sample, which did not pass for hydrothermal treatment, only a large band is observed, without defined peaks. The hydrothermal treatment provided the crystallization of the samples, where the characteristic peaks of $ZnWO_4$ were observed after 5 min, making them peaks became more intense and well defined with the increase of the

Table 1
Microstructural parameters of the ZnWO$_4$ samples obtained by the Rietveld refinement.

	ZW5	ZW10	ZW30	ZW60	ZW120
a (Å)	4.501	4.536	4.689	4.691	4.687
b (Å)	5.846	5.745	5.784	5.763	5.76
c (Å)	5.123	5.166	4.981	4.972	4.969
Cell volume (Å^3)	134.80	134.62	135.09	134.41	134.15
β (°)	86.14	87.716	89.986	90.318	90.52
Crystallite size (Å)	39.83	36.81	82.30	176.76	217.18
Microstrains (ε)	0.0148	0.0153	5.7310^{-4}	2.9510^{-4}	4.5710^{-4}
Crystallization (%)	19.7	21.8	37.7	72.2	100

hydrothermal treatment time. The wavelength applied in this methodology makes the polar molecules and ions orient according to the radiation, providing the simultaneous heating of all solutions. Thus, even in short synthesis times, high pressure in parallel with simultaneous heating leads to crystal formation and growth even in short times [17]. The peaks were characterized according to ICSD 22348 card, with monoclinic structure and spatial group P2/c (No.13) and without secondary phases.

Further information regarding the crystalline structure of the powders was obtained by Rietveld refinement using Maud software [27]. For this, we used background, scale factor, microstructure, crystal, texture and strain parameters for refinement. The crystallinity percentage of the samples was estimated with reference to ZW120 sample since it presents the highest intensity. For this, it was based on the variation of the diffraction peak intensity referring to the plane (111). Table 1 presents the lattice parameters, crystallite size, microstrain and crystalline phase percentage. According to Table 1, it has been that the increase in permanence in the hydrothermal treatment increases the lattice parameter *a* and reduction in *c*, in parallel with the *β* angles increase. The crystallites size was directly influenced by increase in hydrothermal treatment time, as well as by the amount of crystalline phase, where the increase in treatment time increased the crystallite size from 39.83 to 217.18 Å, increasing the residence time from 5 to 120 min. The absence of peaks defined in ZW0 sample made it impossible to obtain more information about it. Hydrothermal treatment times longer than two hours did not provide significant changes in ZnWO$_4$ powders crystallinity. Therefore, they were not considered for discussion.

The FTIR analysis was performed with a scan between 400 and 4000 cm^{-1} to identify the functional groups present in the surface of ZnWO$_4$ samples. The FTIR spectra are shown in Fig. 1b. Bands appearing at wavelengths below 1000 cm^{-1} are usually associated with stretching vibrations between metals and oxygen [28]. The narrow bands appearing between 476 and 576 cm^{-1} refer to the elongation vibrations in octahedral clusters of Zn–O (ZnO$_6$) and W–O (WO$_6$) [29,30]. The bands around 686 and 806 cm^{-1} in ZW60 and ZW120 samples refer to stretching and twist v_3 vibrations between Zn–O–W [31]. The bands between 1120, 1385 and 1649 cm^{-1} present in all samples refer to the C = C, C–O and C–OH bonds from the surfactant (PVP) [32], indicating that not all surfactant was eliminated in the wash after synthesis. Particulate materials are very sensitive to humidity present in the medium, the presence of wide bands at 3100 and 3600 cm^{-1} are associated with adsorbed water molecules on the surfaces of powders [32]. The bands around 2349 cm^{-1} are associated with C–O groups adsorbed to the surface of the powders [33,34].
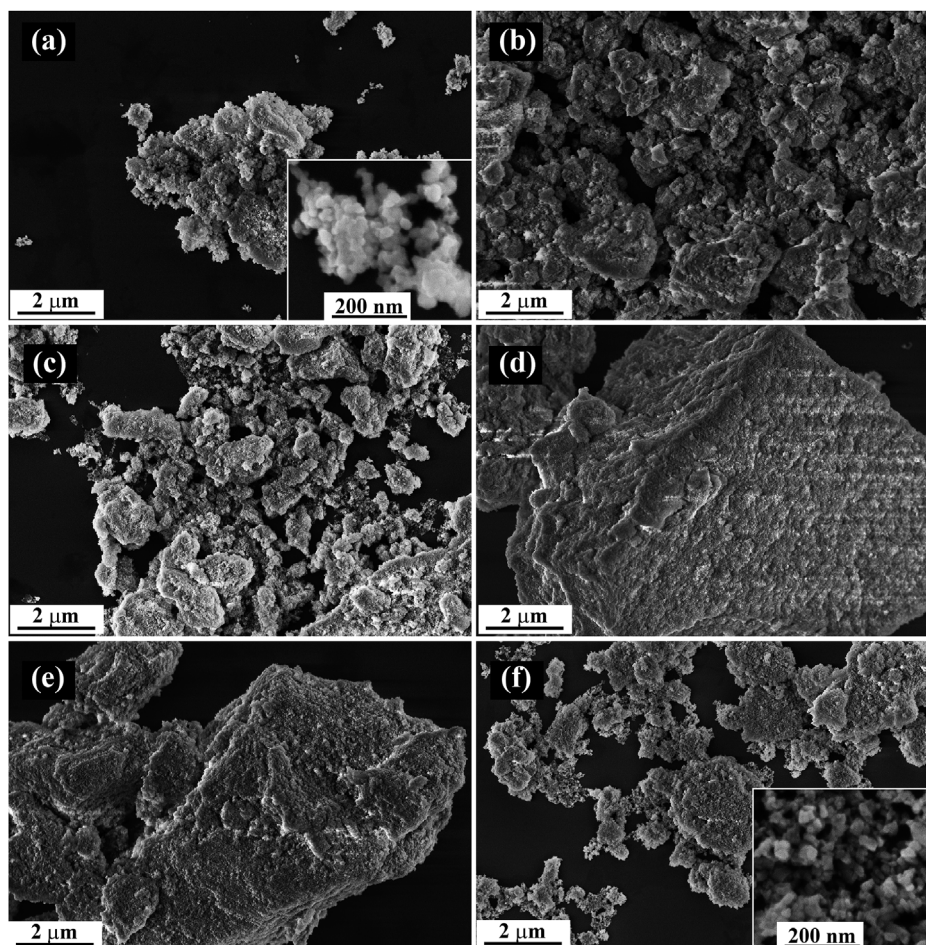

Fig. 2. SEM images obtained for (a) ZW0, (b) ZW5, (c) ZW10, (d) ZW30, (e) ZW60 and (f) ZW120 samples.
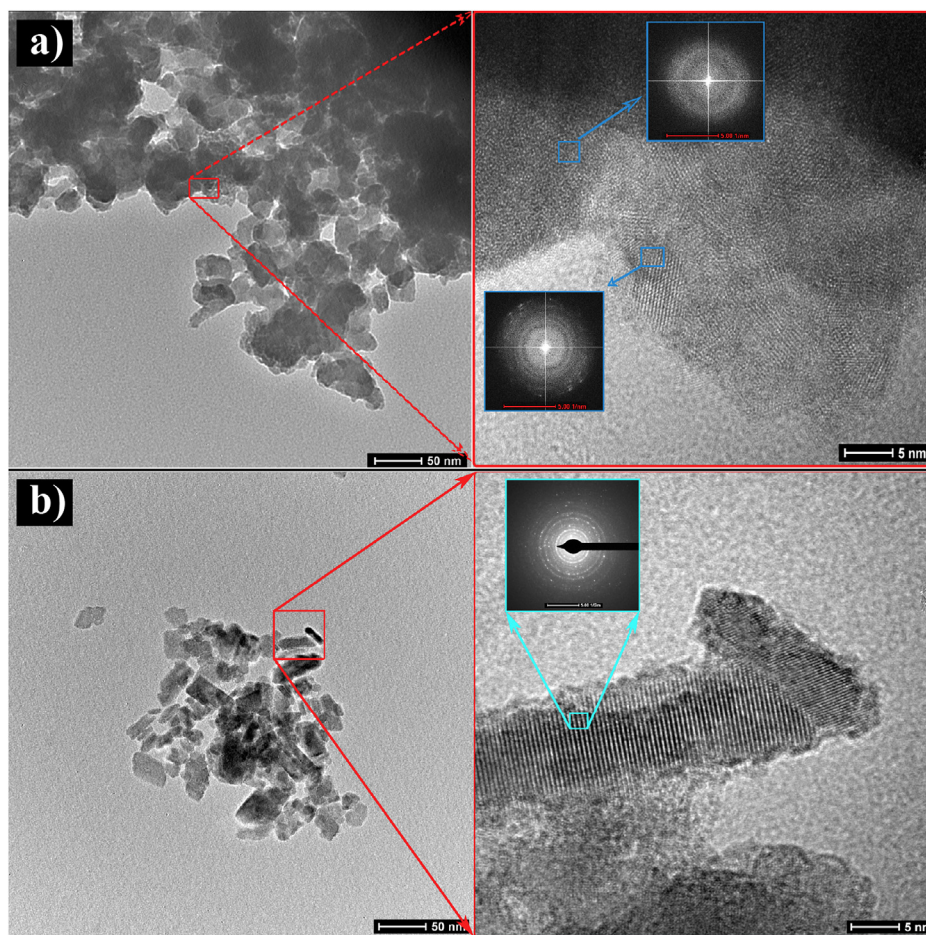
Fig. 3. TEM and HRTEM images for (a) ZN0 and (b) ZN120 samples.

The ZnWO$_4$ nanoparticles morphological analysis was performed by scanning electron microscopy (SEM) and are shown in Fig. 2. Micrographs indicate that nanoparticles have small diameters and high agglomeration. The average nanoparticle diameter was estimated using ImageJ software. For this, at least 200 measurements were performed at different magnifications on ZW0 and ZW120 samples. Fig. S1 shows the histograms of particle size distribution. Even with microwave-assisted hydrothermal treatment for two hours, it is not observed significant changes in nanoparticle diameters, obtaining average values of 28.81 (10.52) and 26.74 (7.55) nm for samples ZW0 and ZW120, respectively. Simultaneous heating of solution due to microwave penetration causes nucleation of several crystalline nuclei simultaneously. These nuclei, upon reaching critical size, grow to form the particles, so that a large amount of particles prevents overgrowth of the others. This fact paralleled the use of surfactant, which interacts with the surface of the particles, reduces their growth and generating particles of small diameters. For a better analysis of the effects of microwave-assisted hydrothermal treatment on ZnWO$_4$ crystallinity and morphology, transmission electron microscopy was performed on ZW0 and ZW120 samples and are shown in Fig. 3. According to Fig. 3a, the ZW0 sample does not present the well-defined crystalline planes, but in some particles, one can see the beginning of crystallization, with the presence of little atomic ordering, as highlighted. On the other hand, Fig. 3b presents the ZW120 sample, with high crystallinity, characterized by the presence of well-defined diffraction planes besides the SAED patterns with well-defined rings, characteristic of the polycrystalline materials. Fig. S2 shows the interplanar spacings for ZW120 sample. According to the values obtained, the ZnWO$_4$ samples have preferential growth in (100) and (111) planes.

Wu et al. [35] showed that the hydrothermal synthesis in autoclave for the time of 20 h at 180 °C generates semi-spherical nanoparticles, with an average diameter of 30 nm. Thus, it can be attributed that low temperatures in parallel with short synthesis times tend to form agglomeration-prone nanoparticles [36]. As the concentration of Zn^{2+} and W^{6+} ions was kept constant and PVP was used as a surfactant, it was expected that the size of nanoparticles would remain close even though the synthesis time varied [37]. Wu et al. [20] synthesized ZnWO$_4$ nanoparticles used CTAB as surfactant through the hydrothermal method and obtained like-leaf morphology. The methodology applied in this work involves low temperature, short synthesis time and surfactant utilization. These three factors have great influence on the formation and growth of the particles. Thus, all these act to prevent the growth of the particles, even in the longest times tested (120 min).

Chemical X-ray fluorescence (XRF) analysis was used for chemical identification of the elements. XRF analysis was performed in ZW60 sample and its spectrum is shown in Fig. 4a. The spectrum shows the transitions related to zinc, tungsten and silicon, where the latter appears due to the substrate used in the analysis. The bands that appear around 8.39, 9.67, 9.96 and 11.28 keV occur due to tungsten Lα, Lβ1, Lβ2 and Lγ1 transition, respectively. The band at 8.63 keV occurs due to zinc kα transition.

The surface area of ZnWO$_4$ powders was estimated by the adsorption of nitrogen on their surface. The adsorption curves are shown in Fig. 4b and the surface area values are shown in Table 2. According to the values obtained, the increase in hydrothermal treatment time reduces the surface area of ZnWO$_4$, varying from 44.12 to 8.16 m^2 g^{-1} for the ZW0 and ZW120 samples, respectively. As seen previously, the hydrothermal treatment time did not promote significant changes in
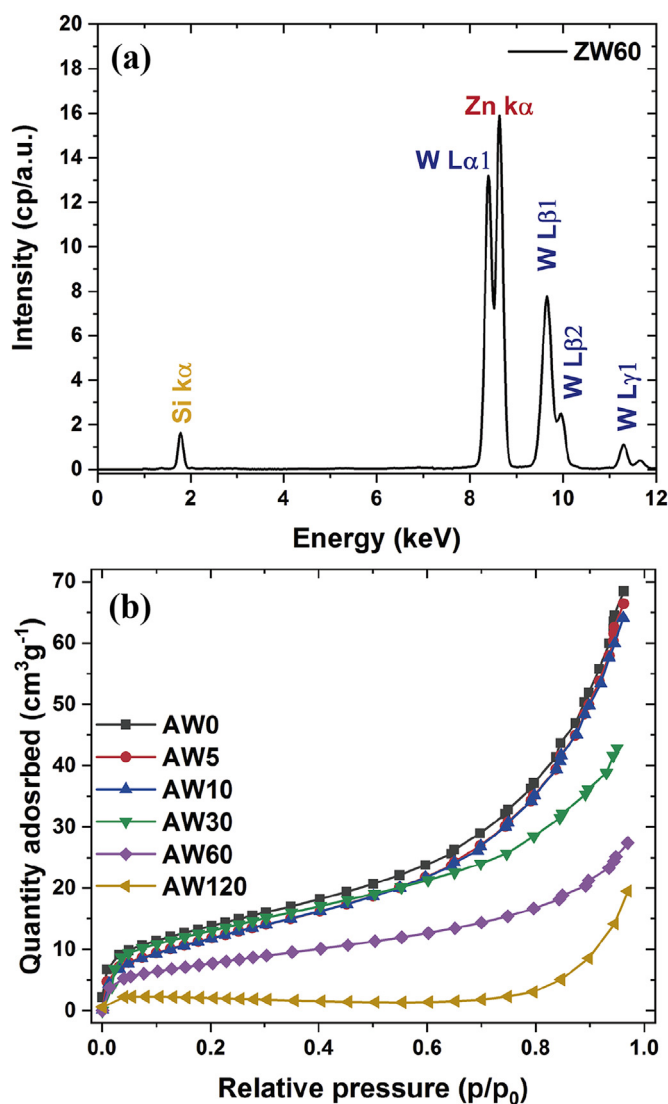
Fig. 4. (a) FRX spectrum for ZW60 sample and (b) adsorption curves for ZnWO₄ samples.

Table 2
Surface area, pore volume, pore diameter and Egap for ZnWO₄ samples.

Analysis	ZW0	ZW5	ZW10	ZW30	ZW60	ZW120
Surface area ($m^2 \cdot g^{-1}$)	44.12	42.52	42.62	42.55	27.58	8.16
Pore volume ($cm^3 \cdot g^{-1}$)	0.1211	0.1028	0.0991	0.0963	0.0424	0.0301
Pore diameter (nm)	14.7861	9.7719	9.6942	9.6664	9.3037	6.1517
Egap (eV)	4.25	4.10	4.04	4.03	4.05	4.04

ZnWO₄ morphology, so the change in the surface area is not attributed to nanoparticle diameter. Thus, the reduction of the surface area with increasing time in hydrothermal treatment is related to the increase of crystallinity of the nanoparticles, as seen through the diffractograms (Fig. 1a), increasing the densification of the samples. As shown in Table 2, the increase in hydrothermal time considerably reduces pore volume, ranging from 0.1211 to 0.0301 $cm^3 \cdot g^{-1}$, and its average sizes, 14.7861 and 6.1517 nm, for the ZW0 and ZW120 samples, respectively. Increased hydrothermal treatment time provides more energy to the system, thus favoring crystal growth and accommodation and reducing particle inherent defects [38].

In this work, short periods of hydrothermal treatments and low temperature were used, causing the system not to receive enough
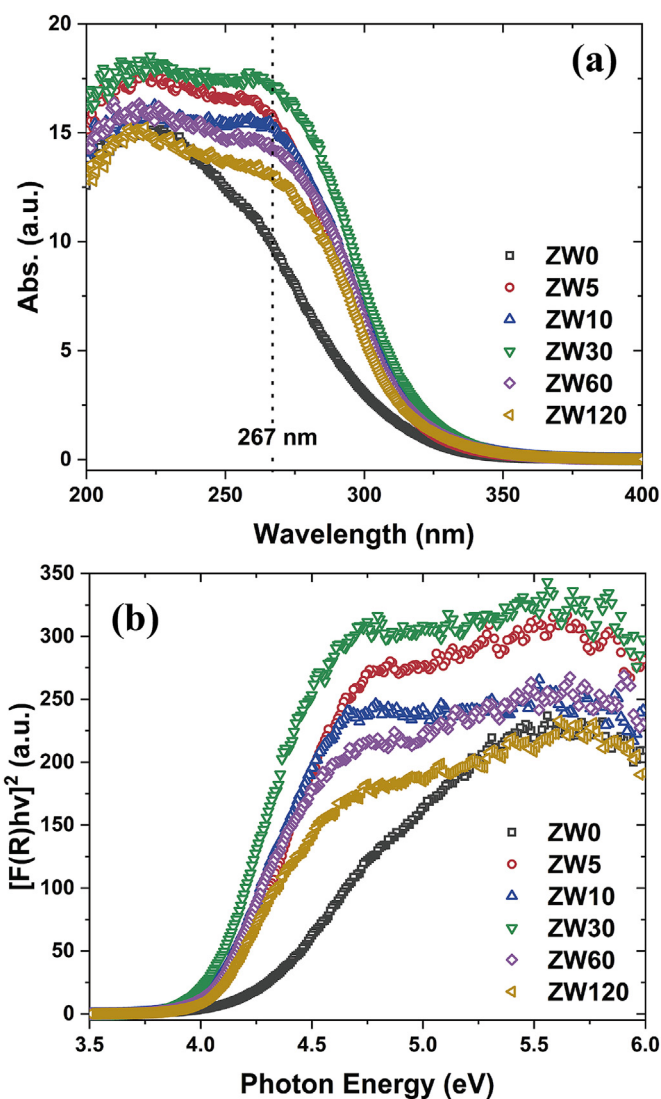

Fig. 5. (a) Absorption spectra and (b) Extrapolation of the linear portion of [F(R)hv]² curve using the Wood and Tauc methodology.

energy for particle growth for a specific morphology, as can be seen comparing with other works in the literature (Table S1). However, as shown in the diffractograms (Fig. 1a) and Table 2, the energy supplied to the system in the times used in this work is sufficient to promote greater crystallization and consequently the reduction of surface defects, leading to a smaller porosity and, consequently, a smaller surface area [38]. In nanomaterials, growth occurs by the formation of particles with small diameters, which due to the high surface energy, agglomerate. When given a certain amount of energy, coalescence occurs and larger particles tend to consume smaller ones by the Ostwald Ripening mechanism [39].

The gap energy (Egap) of the ZnWO₄ powders was estimated by Wood and Tauc [26] methodology to the absorbance data obtained by the Kubelka-Munk [25] function. The absorbance curves are shown in Fig. 5a. For the ZW0 sample, there is the main absorption band around 220 nm. The hydrothermal treatment provides the appearance of a band around 267 nm, indicating the appearance of defects in the band prohibited and requiring lower energy for electrons absorption. As discussed above, the microwave-assisted hydrothermal method provides high crystallization/recrystallization rates, generating defects in the structure of the crystals produced by this method. Huang et al. [13] attributed the alterations in Egap of ZnWO₄ powders obtained by the ultrasonic spray pyrolysis method between 650 and 750 °C to the length
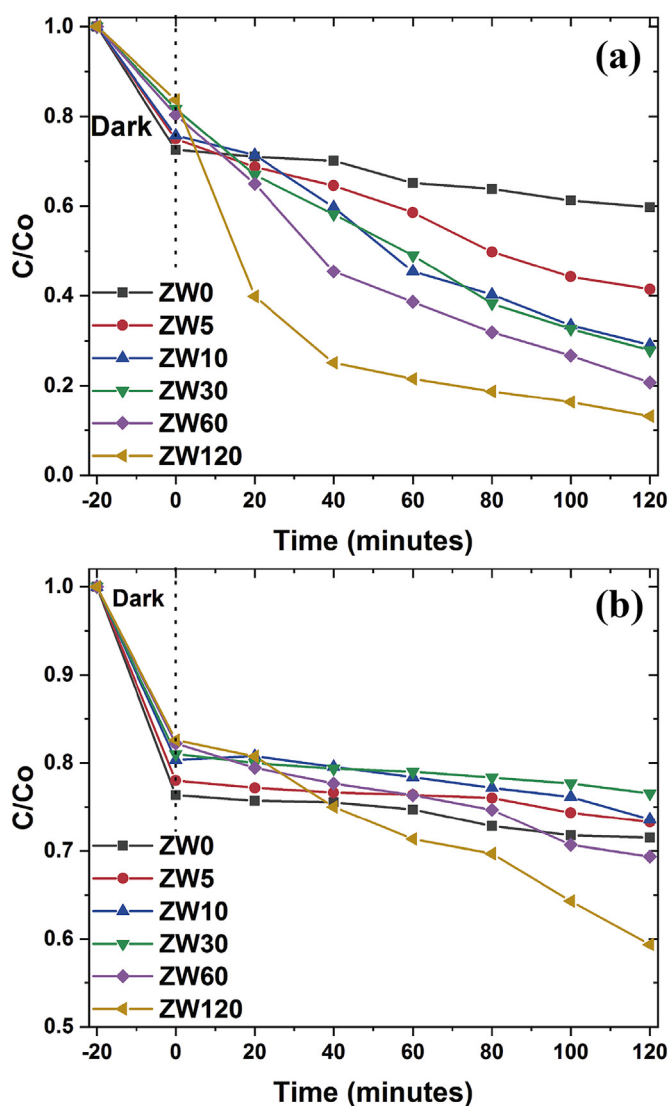
Fig. 6. Concentration variation curves of the (a) MB and (b) MO dyes by the test time for the ZnWO₄ samples.

Fig. 7. Variation curves of methylene blue dye using scavengers: isopropyl alcohol (IA), silver nitrate (AG) and EDTA (ED) compared to the curves without scavengers for the (a) ZW0 and (b) ZW120 samples. (For interpretation of the references to color in this figure legend, the reader is referred to the Web version of this article.)

variation of the bonds between W–O, caused by the variation of the crystal structure. In addition, the appearance of the band at longer wavelengths indicates that more electron/hole pairs (e⁻/h⁺) are photogenerated under light irradiation [20]. Gao et al. [40] showed that ZnWO₄ obtained by the ultrasonic spray pyrolysis (USP) method has absorption below 400 nm, with Bi decoration being an alternative for greater absorption in the visible spectrum region. Fig. 5b presents the curves obtained by the allowed direct transition to gap energy estimate. The obtained Egap values are shown in Table 2. The highest gap energy was obtained for the completely amorphous ZW0 sample, and reduced with the hydrothermal treatment time, remaining practically constant for times greater than 10 min. Amorphous materials do not have long-range organization, so the transition between the valence and conduction bands varies considerably and is generally superior to the same materials in their crystalline form [41,42]. The hydrothermal method provides high crystallization rates, leading to the appearance of defects, which lead to small variations in the Egap of ZnWO₄ powders [43]. The small variation in Egap of powders associated with variation in photocatalytic activity (shown in Fig. 6) indicates that factors associated with crystal structure and surface morphology are the main factors that interfere with photocatalysis, as observed in other works [18,44].

The adsorptive capacity of ZnWO₄ nanoparticles was estimated by maintaining them under agitation with methylene blue (MB) and
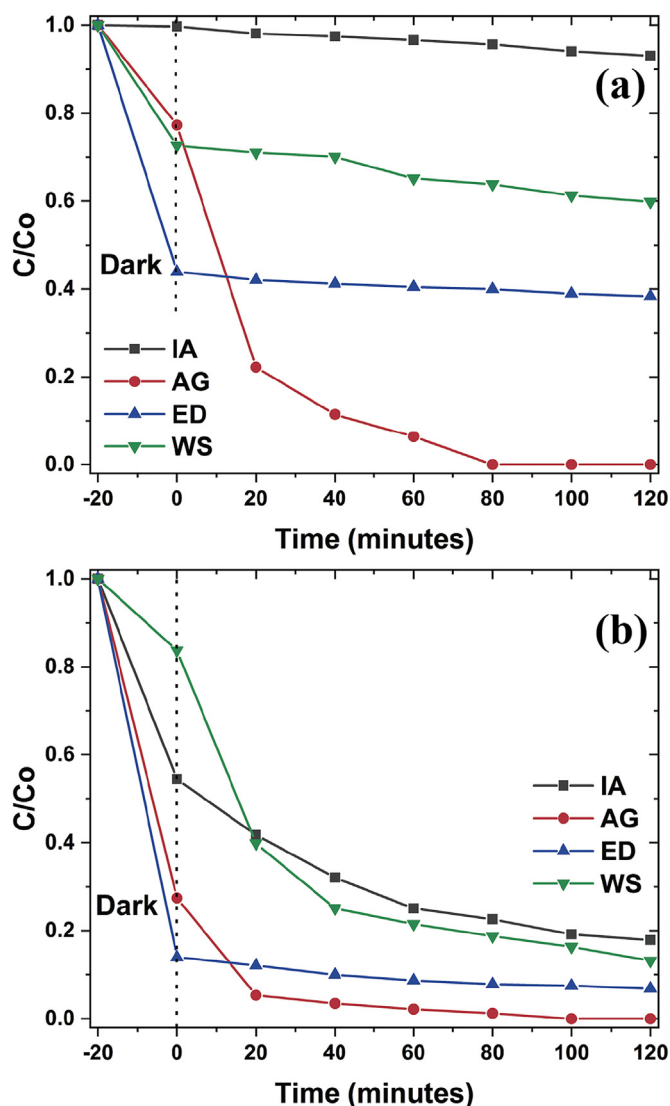
methyl orange (MO) dyes without contact with any source of radiation. Fig. 6 shows the adsorption curves highlighted as "dark". The ZW0 sample presented the best adsorption results, reducing approximately 28% and 24% of MB and MO dye concentration after 20 min. In contrast, the ZW120 sample presented the worst results, reducing only 16% and 17% of MB and MO, respectively. As shown in Table 2, the increase in the hydrothermal treatment time reduces the surface area of the ZnWO₄ nanoparticles, thus reducing their adsorptive capacity.

The photocatalytic activity of the ZnWO₄ powders was estimated similarly to the adsorptive capacity, but the samples were illuminated by UVC radiation (λ = 254 nm) for 120 min. The photocatalytic results indicated an opposite behavior to the adsorbents, where the ZW120 sample reduced the concentration of MB and MO dyes by 87% and 41%, respectively. The photocatalytic capacity against MB dye of the ZnWO₄ powders increased with increasing hydrothermal treatment time, whereas only the ZW60 and ZW120 samples showed remarkable photocatalytic results against the MO dye. Such fact may be related to the formation of oxygen vacancies, where according to Zhang et al. [45], the increase in energy supplied during particle nucleation provides the appearance of oxygen vacancies, which act as centers of impediment in
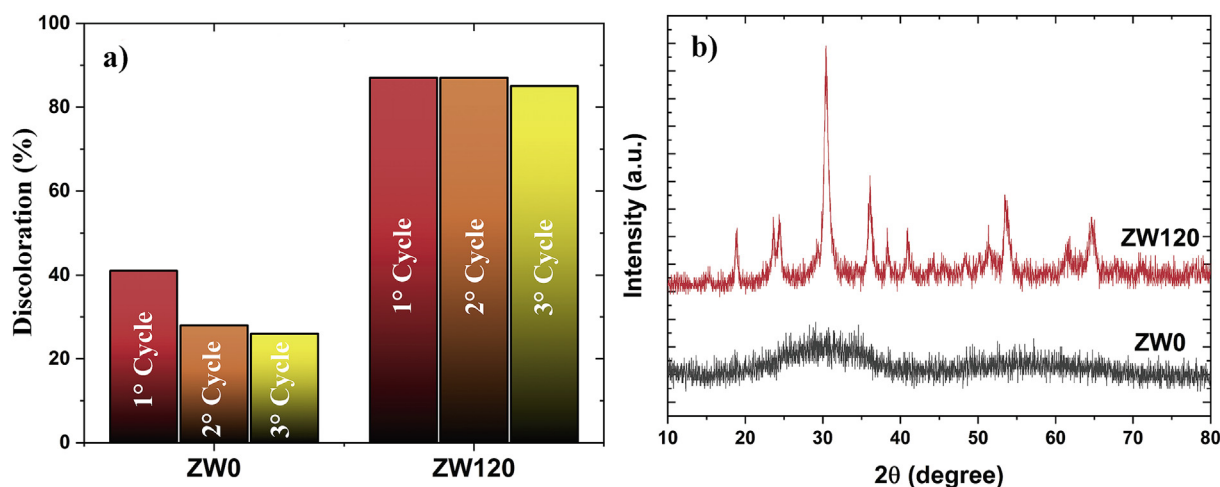
Fig. 8. (a) Variation in discoloration (%) for ZW0 and ZW120 samples for three reuse cycles and (b) XRD after third cycle.

the recombination of electron/hole pairs (e^-/h^+).

The increase in the remaining time in hydrothermal treatment raises the kinetic energy of the atoms in the $ZnWO_4$ lattice, causing the rate of escape of oxygen atoms to increase, being faster than the rate of obtaining atoms of oxygen to the lattice [46,47]. The PL spectra (Fig. S3) show that ZW0 and ZW120 samples have broad bands with maximum intensity in the region of 500 nm, these characteristics being the transitions $^3T_1$, $^3T_2 \rightarrow {}^1A_1$ relative to WO_4^{2-} and WO_6^{6-} groups, respectively [48]. Still according to Fig. S3, it is noticed the band shift to the blue region when performing the hydrothermal treatment in 120 min. It is reported in the literature that oxygen vacancy defects favor emission in the blue region of the visible spectrum [49]. The photoluminescent intensity is associated with the e^-/h^+ pairs photogenerated and recombination rate by the laser incidence, that is, the higher the recombination rate, the higher the emission intensity [50]. Digital photographs of the emissions highlighted in Fig. S3 makes the difference in light intensity visible, both being close to white, characteristic of wide bands that occupy the full spectrum of the visible, confirming the data obtained in the PL curves. It is known that digital photographs can lead to optical illusions, so the CIE graph of these samples was assembled and is shown in Fig. S4. Through the CIE graph, it is clear that the ZW0 sample is located between the blue, green and white colors, while the ZW120 sample near the orange, yellow and white colors, confirming that the oxygen vacancies shift the absorption for the blue region.

The scavengers were used to identify the main mechanisms acting on photocatalysis. For this, the tests against the methylene blue dye were carried out on ZW0 and ZW120 samples, which presented the best and worst photocatalytic result, respectively. Fig. 7 shows the curves of the MB concentration variation by the test time, comparing the use of the scavengers. According to Fig. 7a, it is observed that addition of isopropyl alcohol inhibits the adsorption of the MB dye on the surface of the ZW0, in addition to reducing its photocatalytic activity, reducing MB concentration in 8%. The addition of silver nitrate reduced the adsorptive capacity, in contrast the increased photocatalytic activity. Thus, it has been observed that shorter hydrothermal treatment times increase the recombination rate of the e^-/h^+ pairs, where the inhibition of the electrons leaves a greater number of holes available to act in the oxidation of the MB dye. The high recombination rate is associated with structural disorganization due to its amorphous character [51,52]. The addition of EDTA increased adsorption of the MB dye on the surface of ZW0, but inhibited its photocatalytic activity, indicating that the holes have a great role in the oxidation of MB. The low reduction in photocatalytic activity with the addition of isopropyl alcohol indicates that hydroxyl radicals (˙OH) have a weak influence on the photocatalytic property. Fig. 7b shows the curves of the catalysis mechanisms for the ZW120 sample. The addition of the inhibitors provides an increase in

adsorption of the MB dye on the surface of the particles. The increase in the less expressive adsorption occurred with the addition of isopropyl alcohol, but the photocatalytic behavior remained almost constant, indicating that hydroxyl radicals (˙OH) are not the main photocatalytic mechanism. The addition of EDTA and $AgNO_3$ provided a great increase in adsorption, but inhibited the photocatalytic activity of ZW120, indicating that electrons and holes are the main mechanisms acting on photocatalysis.

Nanoparticulate materials make it necessary to worry about treatment after photocatalysis, as they have a small scale and form a residue that is difficult to treat. Therefore, it is essential that these materials can be used in more than one cycle without complex treatments. In previous work [53], It has been shown that material is ideal for photocatalytic applications when in addition to maintaining photocatalytic efficiency over cycles it is chemically stable with the medium. Reuse tests were then performed, without any heat treatment between cycles, on ZW0 and ZW120 samples against MB dye. Fig. 8 shows the variation in MB dye concentration reduction after 120 min for three consecutive reuse cycles (Fig. 8a) and the diffractogram (Fig. 8b) performed after the third cycle. According to Fig. 8a, the sample ZW0 shows a significant decrease in MB dye discoloration ability with reuse, losing 15% of its efficiency in the third cycle. On the other hand, the ZW120 discoloration capacity remains almost unchanged, losing only about 2% of its efficiency after the third cycle. The diffractograms shown in Fig. 8b indicates the chemical stability of $ZnWO_4$ samples, where there is no secondary phase formation for any sample. Increased noise in diffractograms may be associated with the organic character of MB dye molecules that adsorb on the surface of the powders. Thus, the ZW120 sample is indicated for use in several consecutive cycles for MB dye degradation, maintaining its photocatalytic efficiency even without any treatment between cycles.

4. Conclusions

The microwave assisted-hydrothermal method is a fast and efficient methodology for obtaining high crystallinity $ZnWO_4$ nanoparticles without the presence of secondary phases. The low synthetic times allowed the production of $ZnWO_4$ nanoparticles with a diameter ranging from 31 to 34 nm. The increase in crystallinity, even without altering the diameter of the nanoparticles, reduced the volume of pores and, consequently, the surface area. The increase of the hydrothermal treatment time favors the photocatalytic activity against the cationic dye (MB), whereas the $ZnWO_4$ does not present significant photocatalytic activity against the anionic dye (OM). The increase in the crystallinity acts to favor the photocatalytic activity generated by the electronic excitation, where the charges (h^+ and e^-) show greater

influence than the hydroxyl radicals (˙OH) on the discoloration of the methylene blue dye. The ZW120 sample showed high reuse capacity, maintained your efficiency after three consecutively cycles, thus indicated for applications in several consecutive cycles.

Acknowledgments

This study was partially financed in part by the Coordenação de Aperfeiçoamento de Pessoal de Nível Superior - Brasil (CAPES/PROCAD) - Finance Code 2013/2998/2014 and the authors' thanks the financial support of the Brazilian research financing institution (CNPq) No. 307546/2014 and São Paulo Research Foundation (FAPESP - CDMF) No. 2013/07296-2.

Appendix A. Supplementary data

Supplementary data to this article can be found online at https://doi.org/10.1016/j.ceramint.2019.09.151.

References

[1] M. Mancheva, R. Iordanova, Y. Dimitriev, Mechanochemical synthesis of nanocrystalline ZnWO4 at room temperature, J. Alloy. Comp. 509 (2011) 15–20.
[2] D.P. Dutta, P. Raval, Effect of transition metal ion (Cr3+, Mn2+ and Cu2+) doping on the photocatalytic properties of ZnWO4 nanoparticles, J. Photochem. Photobiol. A Chem. 357 (2018) 193–200.
[3] H. Wang, F.D. Medina, Y.D. Zhou, Q.N. Zhang, Temperature dependence of the polarized Raman spectra of ${\mathrm{ZnWO}}_{4}$ single crystals, Phys. Rev. B 45 (1992) 10356–10362.
[4] A. Kuzmin, J. Purans, Local atomic and electronic structure of tungsten ions in AWO4 crystals of scheelite and wolframite types, Radiat. Meas. 33 (2001) 583–586.
[5] Z. Lou, M. Cocivera, Cathodoluminescence of CaWO4 and SrWO4 thin films prepared by spray pyrolysis, Mater. Res. Bull. 37 (2002) 1573–1582.
[6] P. Siriwong, T. Thongtem, A. Phuruangrat, S. Thongtem, Hydrothermal synthesis, characterization, and optical properties of wolframite ZnWO 4 nanorods, CrystEngComm 13 (2011) 1564–1569.
[7] Z. Hou, C. Li, J. Yang, H. Lian, P. Yang, R. Chai, Z. Cheng, J. Lin, One-dimensional CaWO 4 and CaWO 4: Tb 3+ nanowires and nanotubes: electrospinning preparation and luminescent properties, J. Mater. Chem. 19 (2009) 2737–2746.
[8] S.H. Yu, B. Liu, M.S. Mo, J.H. Huang, X.M. Liu, Y.T. Qian, General synthesis of single-crystal tungstate nanorods/nanowires: a facile, low-temperature solution approach, Adv. Funct. Mater. 13 (2003) 639–647.
[9] M. Bonanni, L. Spanhel, M. Lerch, E. Füglein, G. Müller, F. Jermann, Conversion of colloidal ZnO−WO3 heteroaggregates into strongly blue luminescing ZnWO4 xerogels and films, Chem. Mater. 10 (1998) 304–310.
[10] Z. Lou, J. Hao, M. Cocivera, Luminescence of ZnWO4 and CdWO4 thin films prepared by spray pyrolysis, J. Lumin. 99 (2002) 349–354.
[11] T. Dong, Z. Li, D. Zhengxin, L. Wu, X. Wang, X. Fu, Characterizations and Properties of Eu 3+-doped ZnWO 4 Prepared via a Facile Self-Propagating Combustion Method, (2008).
[12] C. Yu, J.C. Yu, Sonochemical fabrication, characterization and photocatalytic properties of Ag/ZnWO4 nanorod catalyst, Mater. Sci. Eng., B 164 (2009) 16–22.
[13] Y. Huang, Y. Gao, Q. Zhang, J.-j. Cao, R.-j. Huang, W. Ho, S.C. Lee, Hierarchical porous ZnWO4 microspheres synthesized by ultrasonic spray pyrolysis: characterization, mechanistic and photocatalytic NOx removal studies, Appl. Catal. Gen. 515 (2016) 170–178.
[14] N.F. Andrade Neto, P. Zanatta, L.E. Nascimento, R.M. Nascimento, M.R.D. Bomio, F.V. Motta, Characterization and photoluminescent, photocatalytic and antimicrobial properties of boron-doped TiO2 nanoparticles obtained by microwave-assisted solvothermic method, J. Electron. Mater. 48 (2019) 3145–3156.
[15] C.H.R. Paula, N.F. Andrade Neto, L.M.P. Garcia, R.M. Nascimento, C.A. Paskocimas, M.R.D. Bomio, F.V. Motta, Increased degradation capacity of methylene blue dye using Mg-doped ZnO nanoparticles decorated by Ag0 nanoparticles, J. Electron. Mater. 48 (2019) 3017–3025.
[16] G. He, H. Fan, L. Ma, K. Wang, D. Ding, C. Liu, Z. Wang, Synthesis, characterization and optical properties of nanostructured ZnWO4, Mater. Sci. Semicond. Process. 41 (2016) 404–410.
[17] K. Qureshi, M.Z. Ahmad, I.A. Bhatti, M. Zahid, J. Nisar, M. Iqbal, Graphene oxide decorated ZnWO4 architecture synthesis, characterization and photocatalytic activity evaluation, J. Mol. Liq. 285 (2019) 778–789.
[18] K.T.G. Carvalho, O.F. Lopes, D.C. Ferreira, C. Ribeiro, ZnO:ZnWO4 heterostructure with enhanced photocatalytic activity for pollutant degradation in liquid and gas phases, J. Alloy. Comp. 797 (2019) 1299–1309.
[19] U. Alam, A. Khan, D. Bahnemann, M. Muneer, Synthesis of Co doped ZnWO4 for simultaneous oxidation of RhB and reduction of Cr(VI) under UV-light irradiation, J. Environ. Chem. Eng. 6 (2018) 4885–4898.
[20] Y. Wu, S. Zhou, T. He, X. Jin, L. Lun, Photocatalytic activities of ZnWO4 and Bi@ZnWO4 nanorods, Appl. Surf. Sci. 484 (2019) 409–413.
[21] L. Ye, T. Zhang, S. Shao, L. Yang, Y. Cai, W. Guan, Synthesis of poly-o-phenylenediamine (PoPD)/ZnWO4 supported on the fly-ash cenospheres with enhanced photocatalytic performance under visible light, Mater. Lett. 236 (2019) 370–373.
[22] M. Li, Q. Meng, S. Li, F. Li, Q. Zhu, B.-N. Kim, J.-G. Li, Photoluminescent and photocatalytic ZnWO4 nanorods via controlled hydrothermal reaction, Ceram. Int. 45 (2019) 10746–10755.
[23] G.-T. Xiong, W. Zhang, Z.-F. Hu, P.-J. Hu, Y.-M. Pan, Z.-Y. Feng, L. Ma, Y.-H. Wang, L. Luo, Photocatalytic activity of ZnWO4 phosphors doped with Li impurities, J. Lumin. 206 (2019) 370–375.
[24] C.A. Schneider, W.S. Rasband, K.W. Eliceiri, NIH Image to ImageJ: 25 years of image analysis, Nat. Methods 9 (2012) 671–675.
[25] M. Patel, A. Chavda, I. Mukhopadhyay, J. Kim, A. Ray, Nanostructured SnS with Inherent Anisotropic Optical Properties for High Photoactivity, (2015).
[26] B.D. Viezbicke, S. Patel, B.E. Davis, D.P. Birnie Iii, Evaluation of the Tauc method for optical absorption edge determination: ZnO thin films as a model system, Phys. Status Solidi B 252 (2015) 1700–1710.
[27] M. Ferrari, L. Lutterotti, Method for the simultaneous determination of anisotropic residual stresses and texture by x-ray diffraction, J. Appl. Phys. 76 (1994) 7246–7255.
[28] J. Gadsden, Infrared Spectra of Minerals and Related Inorganic Compounds vol. 220, Buttherworth, London, UK, 1975, p. 221.
[29] N.F. Andrade Neto, K.N. Matsui, C.A. Paskocimas, M.R.D. Bomio, F.V. Motta, Study of the photocatalysis and increase of antimicrobial properties of Fe3+ and Pb2+ co-doped ZnO nanoparticles obtained by microwave-assisted hydrothermal method, Mater. Sci. Semicond. Process. 93 (2019) 123–133.
[30] P.F.d.S. Pereira, A. Gouveia, M. Assis, R.C. De Oliveira, I. Pinatti, M. Penha, R. Gonçalves, L. Gracia, J. Andrés, E. Longo, ZnWO 4 nanocrystals: synthesis, morphology, photoluminescence and photocatalytic properties, Phys. Chem. Chem. Phys. 20 (2018) 1923–1937.
[31] G. Huang, Y. Zhu, Synthesis and photocatalytic performance of ZnWO4 catalyst, Mater. Sci. Eng., B 139 (2007) 201–208.
[32] N.F. Andrade Neto, P.M. Oliveira, R.M. Nascimento, C.A. Paskocimas, M.R.D. Bomio, F.V. Motta, Influence of pH on the morphology and photocatalytic activity of CuO obtained by the sonochemical method using different surfactants, Ceram. Int. 45 (2019) 651–658.
[33] S. Husain, L.A. Alkhtaby, E. Giorgetti, A. Zoppi, M.M. Miranda, Effect of Mn doping on structural and optical properties of sol gel derived ZnO nanoparticles, J. Lumin. 145 (2014) 132–137.
[34] S.D. Birajdar, R. Alange, S. More, V. Murumkar, K. Jadhav, Sol-gel auto combustion synthesis, structural and magnetic properties of Mn doped ZnO nanoparticles, Procedia Manuf. 20 (2018) 174–180.
[35] Y. Wu, J. Tie, C. Chen, N. Luo, D. Yang, W. Hu, X. Liu, Synthesis of LAS/ZnO/ZnWO4 3D rod-like heterojunctions with efficient photocatalytic performance: synergistic effects of highly active site exposure and low carrier recombination, Ceram. Int. 45 (11) (2019) 13656–13663.
[36] S.M. Hosseinpour-Mashkani, M. Maddahfar, A. Sobhani-Nasab, Precipitation synthesis, characterization, morphological control, and photocatalyst application of ZnWO4 nanoparticles, J. Electron. Mater. 45 (2016) 3612–3620.
[37] Z. Yanqing, S. Erwei, C. Zhizhan, L. Wenjun, H. Xingfang, Influence of solution concentration on the hydrothermal preparation of titania crystallites, J. Mater. Chem. 11 (2001) 1547–1551.
[38] B.L. Cushing, V.L. Kolesnichenko, C.J. O'Connor, Recent advances in the liquid-phase syntheses of inorganic nanoparticles, Chem. Rev. 104 (2004) 3893–3946.
[39] E.A.C. Ferreira, N.F. Andrade Neto, M.R.D. Bomio, F.V. Motta, Influence of calcination pH on forming silver molybdates obtained by sonochemical method and its application for methylene blue degradation, Ceram. Int. 45 (2019) 11448–11456.
[40] Y. Gao, Y. Huang, Y. Li, Q. Zhang, J.-j. Cao, W. Ho, S.C. Lee, Plasmonic Bi/ZnWO4 microspheres with improved photocatalytic activity on NO removal under visible light, ACS Sustain. Chem. Eng. 4 (2016) 6912–6920.
[41] A. van Dijken, E.A. Meulenkamp, D. Vanmaekelbergh, A. Meijerink, The kinetics of the radiative and nonradiative processes in nanocrystalline ZnO particles upon photoexcitation, J. Phys. Chem. B 104 (2000) 1715–1723.
[42] A.M. Golsheikh, K.Z. Kamali, N.M. Huang, A.K. Zak, Effect of calcination temperature on performance of ZnO nanoparticles for dye-sensitized solar cells, Powder Technol. 329 (2018) 282–287.
[43] M.A. Mahmood, S. Baruah, J. Dutta, Enhanced visible light photocatalysis by manganese doping or rapid crystallization with ZnO nanoparticles, Mater. Chem. Phys. 130 (2011) 531–535.
[44] W. Yan, X. Liu, S. Hou, X. Wang, Study on micro-nanocrystalline structure control and performance of ZnWO4 photocatalysts, Catal. Sci.Technol. 9 (2019) 1141–1153.
[45] H. Zhang, W. Li, G. Qin, H. Ruan, D. Wang, J. Wang, C. Kong, F. Wu, L. Fang, Surface ferromagnetism in ZnO single crystal, Solid State Commun. 292 (2019) 36–39.
[46] S. Kumar, S. Mukherjee, R. Kr Singh, S. Chatterjee, A.K. Ghosh, Structural and optical properties of sol-gel derived nanocrystalline Fe-doped ZnO, J. Appl. Phys. 110 (2011) 103508.
[47] G.H. Mhlongo, O.M. Ntwaeaborwa, H.C. Swart, R.E. Kroon, P. Solarz, W. Ryba-Romanowski, K.T. Hillie, Luminescence dependence of Pr3+ activated SiO2 nanophosphor on Pr3+ concentration, temperature, and ZnO incorporation, J. Phys. Chem. C 115 (2011) 17625–17632.
[48] A. Taoufyq, V. Mauroy, T. Fiorido, F. Guinneton, J.-C. Valmalette, B. Bakiz, A. Benlhachemi, A. Lyoussi, G. Nolibe, J.-R. Gavarri, Photoluminescence properties of CaWO4 and CdWO4 thin films deposited on SiO2/Si substrates, J. Lumin. 215 (2019) 116619.
[49] L. Xu, G. Zheng, F. Xian, Y. Liu, Tailoring the photoluminescent property of ZnO/Ag

nanocomposite thin films based on a thermal treatment, J. Lumin. 198 (2018) 296–301.

[50] J. Xia, H. Li, H. You, Z. Wu, J. Chen, Z. Lu, L. Chen, M. Wang, Y. Jia, Effects of Fe doping on photoluminescent and magnetic properties of CaTiO3:Eu3+, Ceram. Int. 44 (2018) 21530–21532.

[51] J. Yang, Y. Han, J. Luo, K. Leifer, M. Strømme, K. Welch, Synthesis and characterization of amorphous magnesium carbonate nanoparticles, Mater. Chem. Phys. 224 (2019) 301–307.

[52] S.M. Hosseinpour-Mashkani, A. Sobhani-Nasab, A simple sonochemical synthesis and characterization of CdWO4 nanoparticles and its photocatalytic application, J. Mater. Sci. Mater. Electron. 27 (2016) 3240–3244.

[53] N.F. Andrade Neto, Y.G. Oliveira, J.H.O. Nascimento, B.R. Carvalho, M.R.D. Bomio, F.V. Motta, Synthesis, characterization, optical properties investigation and reusability photocatalyst capacity of AgCl-xGO composite, J. Mater. Sci. Mater. Electron. 30 (2019) 15214–15223.